Predictive models for fatigue property of laser powder bed fusion stainless steel 316L

Zhang, M, Sun, C-N, Zhang, X, Wei, J, Hardacre, D & Li, H

Author post-print (accepted) deposited by Coventry University's Repository

Original citation & hyperlink:
Zhang, M, Sun, C-N, Zhang, X, Wei, J, Hardacre, D & Li, H 2018, 'Predictive models for fatigue property of laser powder bed fusion stainless steel 316L' *Materials & Design*, vol 145, pp. 42-54
https://dx.doi.org/10.1016/j.matdes.2018.02.054

DOI 10.1016/j.matdes.2018.02.054
ISSN 0261-3069
ESSN 0264-1275

Publisher: Elsevier

NOTICE: this is the author's version of a work that was accepted for publication in *Materials & Design*. Changes resulting from the publishing process, such as peer review, editing, corrections, structural formatting, and other quality control mechanisms may not be reflected in this document. Changes may have been made to this work since it was submitted for publication. A definitive version was subsequently published in *Materials & Design*, [145, (2018)] DOI: 10.1016/j.matdes.2018.02.054

© 2018, Elsevier. Licensed under the Creative Commons Attribution-NonCommercial-NoDerivatives 4.0 International
http://creativecommons.org/licenses/by-nc-nd/4.0/

Copyright © and Moral Rights are retained by the author(s) and/ or other copyright owners. A copy can be downloaded for personal non-commercial research or study, without prior permission or charge. This item cannot be reproduced or quoted extensively from without first obtaining permission in writing from the copyright holder(s). The content must not be changed in any way or sold commercially in any format or medium without the formal permission of the copyright holders.

This document is the author's post-print version, incorporating any revisions agreed during the peer-review process. Some differences between the published version and this version may remain and you are advised to consult the published version if you wish to cite from it.

Published in *Materials and Design*, 145 (2018) 42–54 | doi: https://doi.org/10.1016/j.matdes.2018.02.054

Predictive models for fatigue property of laser powder bed fusion stainless steel 316L

Meng Zhang[1,2], Chen-Nan Sun[3], Xiang Zhang[4], Jun Wei[3], David Hardacre[2], Hua Li[1*]

[1] *Singapore Centre for 3D Printing, School of Mechanical and Aerospace Engineering, Nanyang Technological University, 50 Nanyang Avenue, Singapore 639798*
[2] *Lloyd's Register Global Technology Centre, 1 Fusionopolis Place, #09-11 Galaxis, Singapore 13852*
[3] *Singapore Institute of Manufacturing Technology, ASTAR, 73 Nanyang Drive, Singapore 637662*
[4] *Faculty of Engineering, Environment & Computing, Coventry University, Coventry CV1 5FB, UK*
**Corresponding author: lihua@ntu.edu.sg*

Abstract

The selection of appropriate processing parameters is crucial for producing parts with target properties via the laser powder bed fusion (L-PBF) process. In this work, the fatigue properties of L-PBF stainless steel 316L under controlled changes in laser power and scan speed were studied by employing the statistical response surface method. Processing regions corresponding to different fatigue failure mechanisms were identified. The optimum fatigue properties are associated with crack initiation from microstructure defect, which, by acting as the weakest link, creates enhanced porosity-tolerance at applied stress approaching the fatigue limit. Deviations from the optimum processing condition lead to strength degradation and porosity-driven cracking. Based on the observed relations between microstructural features and failure behaviour, a processing-independent fatigue prediction model was proposed. The microstructure-driven failure was modelled by a reference *S-N* curve where the intrinsic effect of microstructure inhomogeneity was accounted for by applying a reduction factor on fatigue life. For the porosity-driven failure, high cycle fatigue life follows an inverse-square-root relation with porosity fraction. This relation was incorporated into the Basquin equation for predicting the fatigue strength parameters.

Keywords: fatigue; porosity; predictive model; Basquin equation; stainless steel 316L; selective laser melting

1. Introduction

Laser powder bed fusion (L-PBF) is a popular additive manufacturing technique for fabricating metal parts. Micro-layers of metal powder are fused using high power laser which traces part geometry based on input from three-dimensional digital models. It is a complex, non-linear system controlled by a large number of processing parameters, expanding from laser unit, powder feedstock, processing parameters to chamber environment, etc. Transfer of processing knowledge across different L-PBF systems is often limited as these systems are developed independently based on a large amount of experimental data. Understanding of processing capability beyond the established standard processing conditions is lacking but desirable, as it allows better property control at the upstream processing stage as well as for downstream property assessment and qualification.

Not all L-PBF variables are significant for mapping the processing-property relationship, as according to the Pareto principle, generally about 20% of the inputs of a system are responsible for 80% of the outcomes. Physics-based and data-driven methods have been employed for determining the key process variables via evaluation of response indicators such as track characteristics and mechanical properties. For the data-driven approach, traditional design of experiment analysis exploits controllable parameters such as laser power, scan speed, layer thickness, etc. for process optimisation [1-5]. Advanced machine learning methods have also been leveraged for parameter selection and developing new processing domains using existing processing and material knowledge [6-8].

Of the physical and mechanical properties of L-PBF materials, fatigue is an important but less well-studied aspect, especially in terms of the influence of processing condition. Build orientation is one of the variables that has been researched for a number of L-PBF materials such as Ti-6Al-4V [9, 10], AlSi10Mg [11] and iron-based alloys [12-14]. Results from these and other works [15, 16] show that, despite the use of standard or optimised processing strategies, large lack of fusion pores are the detrimental defect that trigger fatigue crack initiation. As such defects are often generated due to poor inter-track or -layer bonding under insufficient energy input [17], it becomes questionable if critical fatigue defects are unavoidable using current established processing conditions. The relations between processing and defects, as well as defects and fatigue property, need to be clarified before fair comparisons can be made with regards to the fatigue resistance of L-PBF materials vis-à-vis the conventional wrought or cast forms.

Constructing an effective database based on data from existing research to answer this question is not feasible, as different L-PBF systems and processing domains are used in these studies. This work aims to provide preliminary data for a systematic examination of the L-PBF processing-structure-property relations. The influence of laser power and scan speed on the fatigue properties of stainless steel 316L, an alloy used in many fatigue-critical applications, were evaluated. Regions of processing variable space, where different failure mechanisms could be expected, were identified. In addition, by focusing on the structure-property relations, a processing-independent model was developed which circumvents the processing factor and allows better transferability of data across L-PBF systems.

2. Materials and experimental methods

2.1 Sample fabrication and processing parameter selection

Samples were fabricated from commercially available stainless steel 316L powder, with a predominantly spherical shape, on an L-PBF system (EOS M290). Rectangular test blocks for mechanical tests and microstructure characterisation were produced by varying laser power P and scan speed v, according to the central composite design (CCD) shown in Figure 1, at 20 μm layer thickness on a preheated platform. The CCD is an effective design architecture for modelling second-order systems [18], which were found to successfully represent the relations between processing parameters and porosity [3, 4] and mechanical properties [19] of L-PBF materials. The working range was determined to prevent build failure, especially under the high input energy condition where part deformation due to excessive thermal residual stress could result in recoater blade damage and termination of the build job. The centre point S1 is the optimised processing condition according to the manufacturer's recommendation.

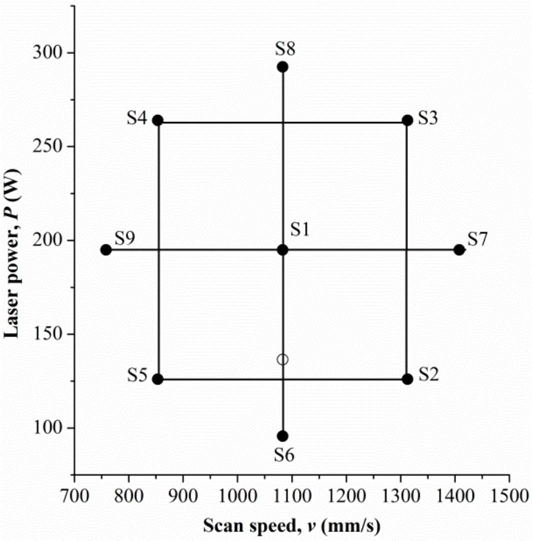

Figure 1 Sample design points labelled as S1-S9. The unfilled dot indicates the confirmation run.

2.2 Mechanical test and microstructure analysis

Samples for mechanical tests were sliced from as-built test blocks such that the loading axis was perpendicular to the build direction. They were machined by electric discharge machining (EDM) wire cutting, in accordance to geometry requirements of the ASTM E466, into flat specimens with thickness 3 mm, gauge length 14 mm, width 7 mm, and overall length 119 mm. Specimens were manually grinded to remove residual surface oxides generated from the EDM process before performing mechanical tests. Load-controlled fatigue tests were carried out under sinusoidal loading at load ratio R = 0.1 and frequency of 5 Hz on an MTS 810 hydraulic testing machine. Specimens that did not fail after 10^6 cycles were considered as run-outs. Static tensile tests were carried out in displacement-controlled mode with a crosshead speed of 0.2 mm/min on a universal testing machine.

Porosity fraction was determined from image analysis of optical micrographs taken on polished sections parallel to the build direction. Maximum pore size distributions were determined by taking at least 30 random images for each specimen, where the largest pore area from each image was used as the input for fitting the Gumbel Extreme Value Distribution by the maximum likelihood method, in accordance with the ASTM E2283 for extreme value analysis of non-metallic inclusions. The location and scale parameters of the distribution were then used for calculating the mean and standard deviation of the extreme pore size according to standard formulae. Circular pores were assumed, as based on works by Murakami [20], the maximum stress intensity factor at the crack front of an irregularly shaped defect is proportional to the square root of the defect area projected on to a plane that is normal to the applied stress. This approach had been successfully adopted for fatigue modelling [21] and was used in this work for quantifying pore size, i.e. the equivalent circular diameter. The location of defects, which is also an important parameter for fatigue failure [22], was not considered as fractography inspection showed that major crack origins were always close to the specimen surface.

2.3 Statistical analysis

Regression models were developed for the output response fatigue life N at two loading conditions: high stress loading with stress amplitude σ_a = 296 MPa and low stress loading with σ_a = 197 MPa. As 10^5 cycles is generally used as a crude estimation of the division between high and low cycle fatigue for the stress-life approach [23], these stress levels were selected accordingly for examining the low cycle and high cycle fatigue properties respectively. However, it is to be noted that for some specimens, fatigue life did not fit exactly according to the 10^5 cycles criterion. For all design points, at least two specimens were tested at each loading.

The commercial software Design-Expert® was used for performing statistical analysis and deriving the response surface models. The coded levels of the process variables were used in the analysis, where the upper limits of the variables were coded as 1.414 and the lower limits as -1.414. Significant model factors were identified by analysis of variance (ANOVA).

3. Results and discussion

3.1 Regression model and statistical analysis

The response variable N in terms of the number of cycles to failure was fitted to the experimental data by second-order polynomial equations:

$$N_{low\ stress} = 5873000 - 23626P - 11127v + 56.113Pv - 20.726P^2 + 4.6835v^2 - 0.023610Pv^2 \tag{1}$$

$$N_{high\ stress} = 760850 - 3349.9P - 1445.3v + 8.6571Pv - 4.4993P^2 + 0.56325v^2 - 0.0035038Pv^2 \tag{2}$$

Table 1 displays the p-values of the regression models. Terms with Prob > F (p-value) smaller than 0.05 are significant factors and were included in the regression models. For the low stress fatigue life model, insignificant terms such as v and v^2 were retained to preserve model hierarchy, which is required for conversion between the coded and natural variables.

Table 1 List of p-values for the model terms and lack of fit determined from ANOVA.

	Model	***P***	***v***	***Pv***	***P*²**	***v*²**	***Pv*²**	**Lack-of-fit**
$N_{\text{low stress}}$	<0.001	<0.001	0.863	0.004	<0.001	0.856	0.019	0.070
$N_{\text{high stress}}$	<0.001	<0.001	<0.001	<0.001	<0.001	<0.001	<0.001	0.898

The low stress model exhibits more significant lack-of-fit (smaller p-value), indicating poorer fitting of the experimental data. This is in agreement with the fitting results shown in Table 2, where the value of R^2 for the low stress model is smaller, at 0.733. However, adding additional term, i.e. P^2v, to the low stress model only marginally improved the adjusted R^2, a parameter that takes into consideration the effect of additional terms on model fitting, to 0.765. Besides, the predicted R^2, which evaluates the performance of the model for predicting responses for new observations, also improves only slightly (to 0.595) after adding the new term. Thus, P^2v was not included in the second-order model to prevent overfitting. As the R^2 values are reasonable, and the predicted R^2 of the current models are in good agreement with the adjusted R^2, i.e. less than 0.2 difference, and the adequate precision is large, i.e. more than 4, the models can be considered to have good signal-to-noise ratio and predictive capability for navigating the tested variable space.

Figure 2 shows the normal probability plots of the residuals. An inspection of the plots shows that the data points fit generally well to the straight lines such that the normality assumption is valid.

Table 2 Fit statistics of the models.

	R^2	Adjusted R^2	Predicted R^2	Adequate precision
$N_{\text{low stress}}$	0.809	0.733	0.586	8.832
$N_{\text{high stress}}$	0.985	0.975	0.954	30.071

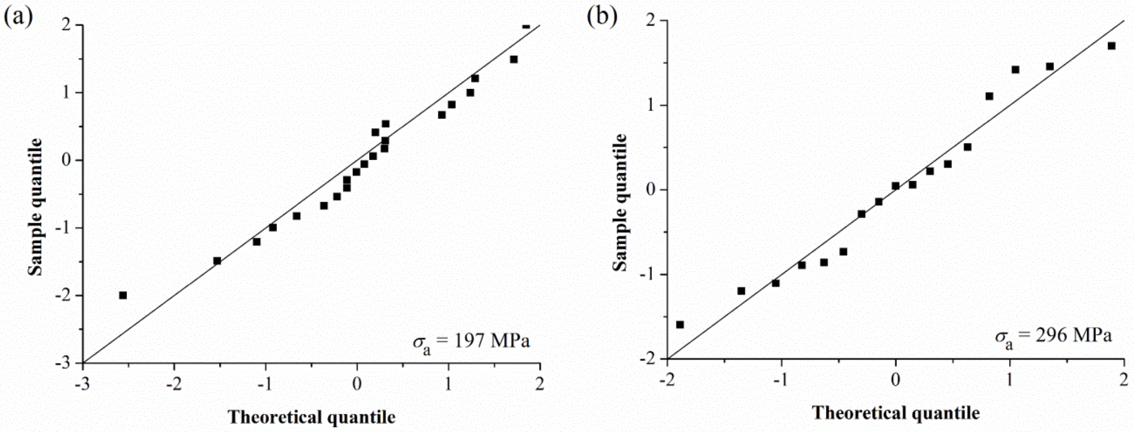

Figure 2 Normal probability plots of the fatigue life residuals for the (a) low stress and (b) high stress conditions.

In summary, Equations (1) and (2) can be used for modelling fatigue life within the current working range. The second-order regression model exhibits very good predictive power for fatigue life under high stress conditions. At lower stress or higher fatigue life, performance is not as good and could be improved by employing higher-order models.

3.2 Processing regions

Figure 3 shows the fatigue life contour plots. As several measurements were made for each of the design points and the regression equations are optimal but not exact fits to the data (as shown by the fit statistics in Table 2), the lower 95% confidence regions of the centre point were drawn in dash lines to provide an indication of the size of the statistical error margin. The optimum processing region occurs in the diagonal direction such that combinations of high *P* and low *v* as well as low *P* and high *v* result in lower fatigue life. Besides, small *P* and *v* appears to be more favourable for longer fatigue life as indicated by the contour lines forming a ridge where the peak contours were predicted at the lower left end of the graphs, potentially beyond the current working range.

Contrasting the two loading conditions, scan speed has a weaker effect on the low stress fatigue life as shown by the contour lines being stretched more in the direction of the horizontal axis. This has also been demonstrated by results from ANOVA where p-values for terms involving *v* are not significant for the low stress model. This result can be interpreted in two ways. First, the effect of processing on fatigue life under low stress is masked by the larger amount of inherent data scatter, which is consistent with the general understanding that data scatter increases as the fatigue limit is approached [24]. For example, in Figure 3a, both S3 and S7 lie in the 95% confidence region, such that any difference in response is not directly distinguishable from the prediction error. However, in Figure 3b, their reduction in fatigue life is considerable in comparison with the error margin, indicating a true difference in the response. Second, fatigue life under low stress could be either more or less sensitive to processing due to effects of process-induced microstructure on the fracture mechanism, which is not reflected on the response surface plots. The more significant lack-of-fit is an indication that the second-order model is inadequate for modelling the intricate relations between processing and low stress fatigue life. The cause of the observed behaviour was investigated by fractography analysis. Figure 3c maps the *P*-*v* diagram into the optimum, over-melt and under-melt regions; various types of defect that are critical for the failure of the specimens were identified. The following sections describe the fracture behaviour and the relative effect of the defects on fatigue life in detail.

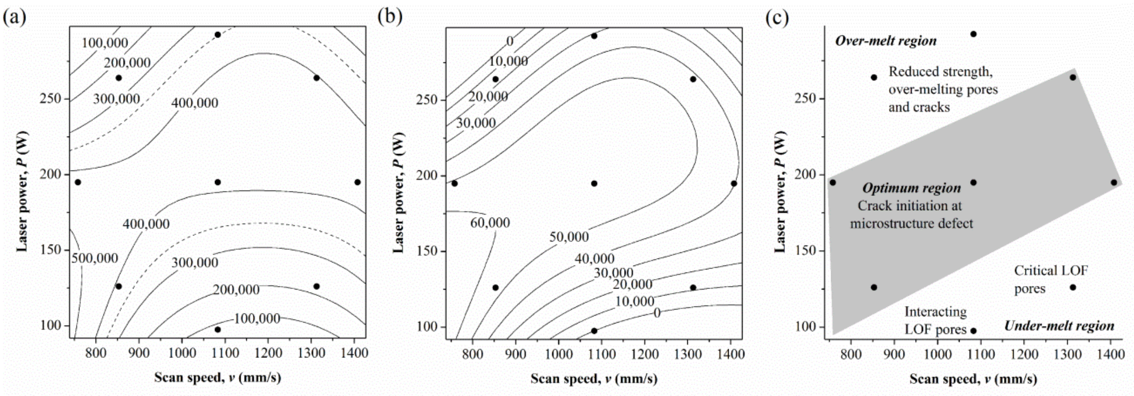

Figure 3 Contour plots of (a) low stress fatigue life and (b) high stress fatigue life in terms of laser power and scan speed; (c) processing regions in terms of the critical defects on fatigue life. [Note: Dots indicate the sample design points S1 – S9 as labelled in Figure 1; dotted lines mark the lower 95% confidence region of the centre point; LOF stands for lack of fusion.]

3.2.1 Optimum processing

Figure 4a-c shows the fractographs of S5, which illustrate the fatigue fracture behaviour of L-PBF stainless steel 316L under the optimum processing condition. Under high stress, fatigue crack develops with a considerable area of stable crack propagation (Figure 4a). Intergranular crack initiation took place at solidification dendrite boundaries close to the specimen surface (Figure 4b), as well as in the interior of the specimen (Figure 4b), forming secondary crack origins.

In L-PBF processing, competitive grain growth during rapid cooling produces differently-oriented grain clusters and sharp angle areas [25, 26], which are heavily stressed sites that promote intergranular fracture via the mechanism of slip/grain boundary interaction [27, 28]. Second phase particles such as oxide nano-inclusions were found to line the sub-grain boundaries [29] and could create stress concentration sites that promote intergranular cracking. Under the high applied stress, grain boundary defects in the bulk of the material could also develop into cracks such that failure traces back to multiple intergranular crack origins.

Such fracture behaviour applies to a range of processing conditions as marked in Figure 3c. Average equivalent circular pore diameter in these samples, as determined from the extreme value analysis, are on the order of 10 μm. They are mainly spherical gas pores generated by the trapping of chamber gas or impurities within the raw powder [30]. Some small lack of fusion defects, with average size of about 19 μm, were also detected in S7, but they did not constitute the primary crack origins. Microstructure defects create stronger stress concentration effect such that lack of fusion pores of this size are not critical to crack initiation.

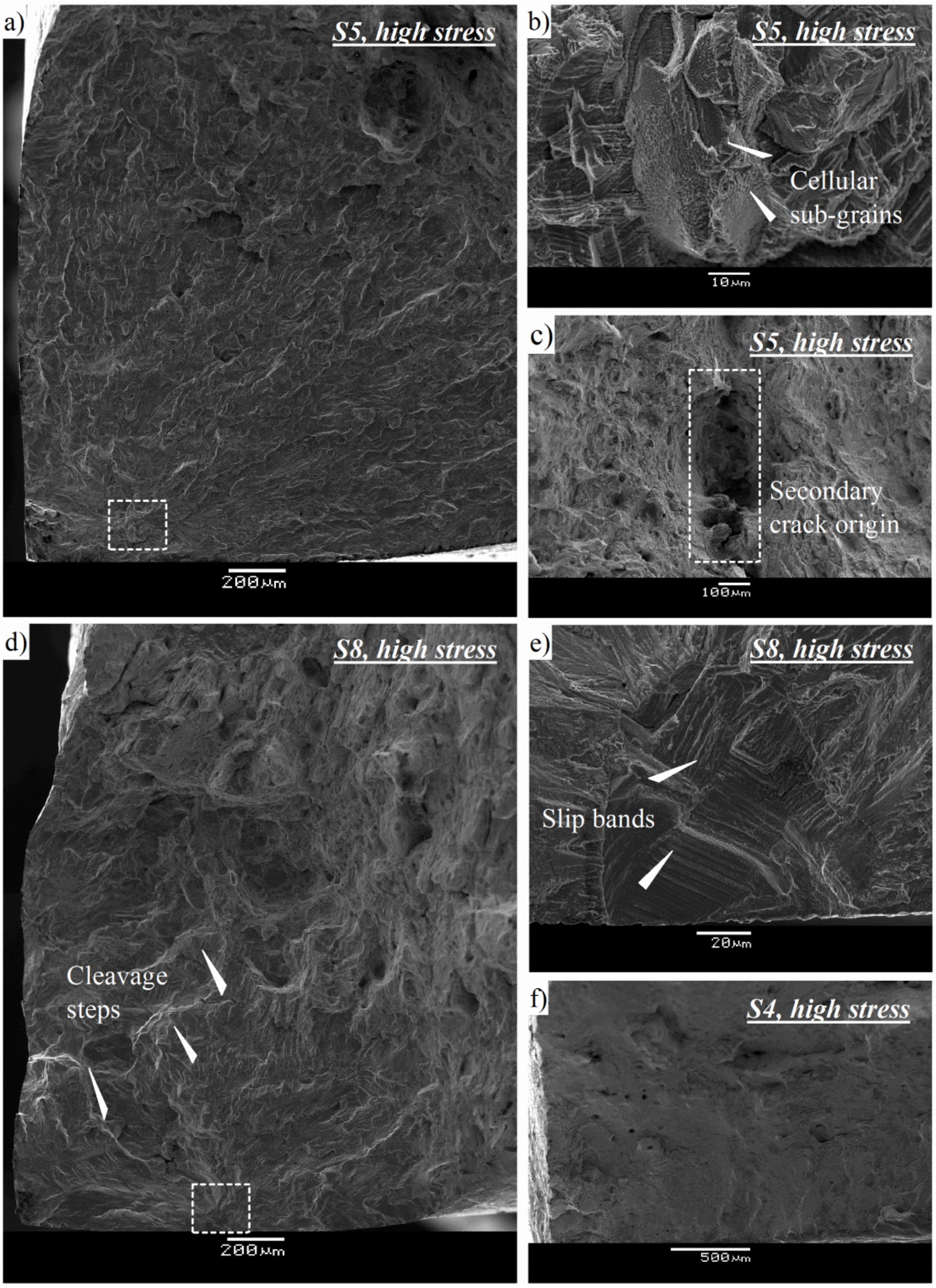

Figure 4 SEM fracture images of S5 (a-c), S8 (d-e) and S4 (f) under the high applied cyclic stress. (a) Large area of stable crack propagation in S5; (b) enlarged view of the boxed region in (a) showing intergranular crack initiation via de-bonding at cellular sub-grains; (c) secondary intergranular crack initiation site in the bulk material; (d) unstable crack propagation containing cleavage steps; (e) enlarged view of the boxed region in (d) showing transgranular crack initiation and slip bands; (f) featureless fracture profile due to the static ductile fracture mode.

3.2.2 Over-melting effect

Figure 4d-f shows fractographs of the over-melted samples S4 and S8. Comparing Figure 4d with Figure 4a, unstable crack propagation occurred in S8, whose fracture surface consists of large cleavage steps and a rugged morphology. In contrary to the grain boundary cracking in S5, crack initiation occurred by the transgranular mode, as shown in Figure 4e.

Figure 4f shows that S4 failed via the static mode of dimple rupture with no distinct crack origin. Over-melting led to significantly reduced material strength such that the applied load exceeded the yield strength of the material. Nonetheless, under the low stress condition, the same transition in crack initiation mechanism (from intergranular to transgranular cracking) is applicable, as shown in Figure 5. It can be seen that S5 contains a large intergranular crack initiation region on the order of 100 μm (Figure 5a-b), whereas crack initiation in S4 is transgranular (Figure 5c-d). Arrows in Figure 5d trace the grain boundaries, where instead of sliding along the grain boundary as in Figure 5b, cracking took place through the grains.

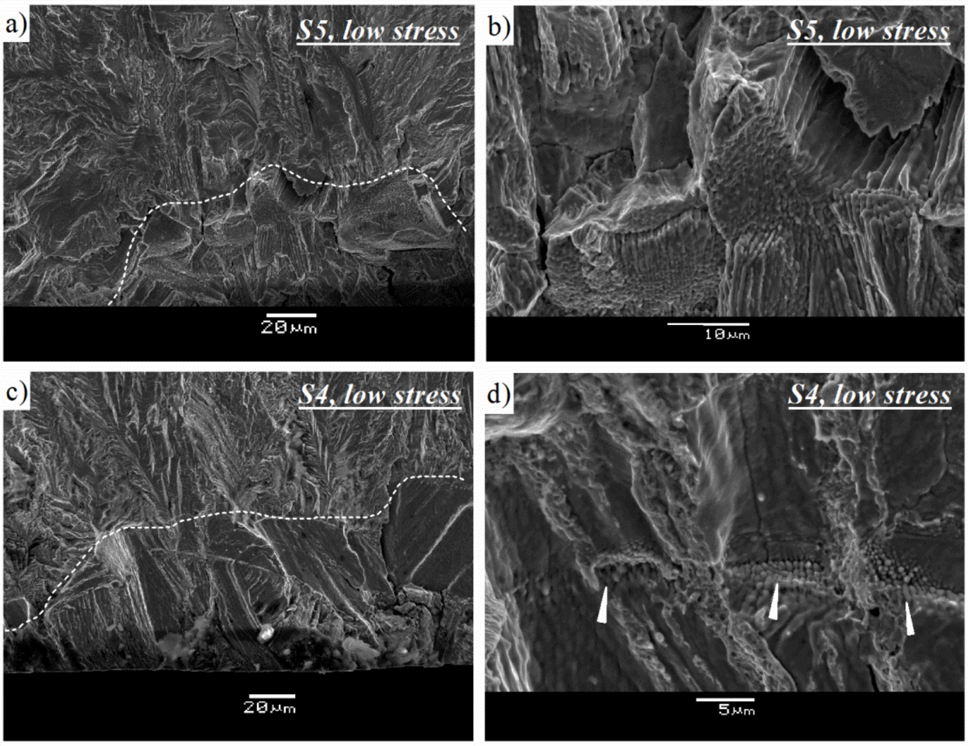

Figure 5 SEM fracture images, under the low applied cyclic stress, of (a) crack initiation zone in S5; (b) enlarged view of (a) showing cellular sub-grains revealed due to intergranular cracking; (c) crack initiation zone in S4; (d) enlarged view of (c) showing transgranular cracking through grains (arrows indicate grain boundaries).

Processing conditions associated with over-melting could impact fatigue resistance in ways such as: 1) degraded material strength due to grain coarsening and vaporisation of volatile allying element, e.g. Manganese in stainless steel 316L [31-33]; 2) increased crack density due to porosity, e.g. caused by keyhole-mode laser melting [34] and intense spattering [35], and thermal cracks due to residual stress in the bulk material [36]. The first case is more applicable to the current processing conditions, as pores were not detected at the crack origins of the samples, except for a few S8 samples, where pores on the order of 40 μm were found (refer to the authors' prior work [37] for details). In addition, as keyholes pores are usually found at the edges of the scan tracks [38], which were removed by the machining process, the influence of over-melting-induced pores are not the dominating causes for crack initiations in S4 and S8.

In terms of the effect of material strength on fatigue properties, it is known that both low scan speed and high laser power reduce cooling rate [39], which impacts sub-grain size significantly by causing grain coarsening [40]. This, besides affecting the load-bearing capacity, also affects the distribution of second phase particles and the fracture behaviour. Specifically, lower cooling rate in L-PBF processing was found to be related to the transition from intergranular to transgranular fatigue crack initiation [37], as the larger dendritic arm spacing facilities the trapping of particles between intercellular spacing rather than grain boundaries [41]. As a result, slip occurs more readily across the dendrite cells, causing the observed transgranular cracking. As fracture path is shorter for transgranular cracking, fatigue resistance could be reduced. Simultaneous cracking created the higher crack density and disturbance to the major crack front, where the linking of individual cracks produced the stepped fracture profile and lower fatigue life.

3.2.3 Under-melting effect

Reducing energy input from the optimum condition creates lack of fusion defects that trigger fatigue crack initiation. Figure 6 shows porosity-dominated failure in S2 and S6. Under low stress, crack initiation could be traced to lack of fusion pores at the surface of S2 (Figure 6a). Interior pores, as indicated by arrows, could have caused localised cracking, but propagation of the major crack front is still transgranular and stable. For S6, no distinct major crack origin could be found (Figure 6c). Brittle rupture occurred via the joining of large and interconnected pores.

Under high stress, even S2 exhibited catastrophic failure. As shown in Figure 6b, no stable crack propagation could be found adjacent to the crack origin. Ductile failure involving the coalescence of micro-voids dominates areas between large pores. In this case, overloading occurred since the load-bearing area was significantly reduced by the presence of the lack of fusion pores.

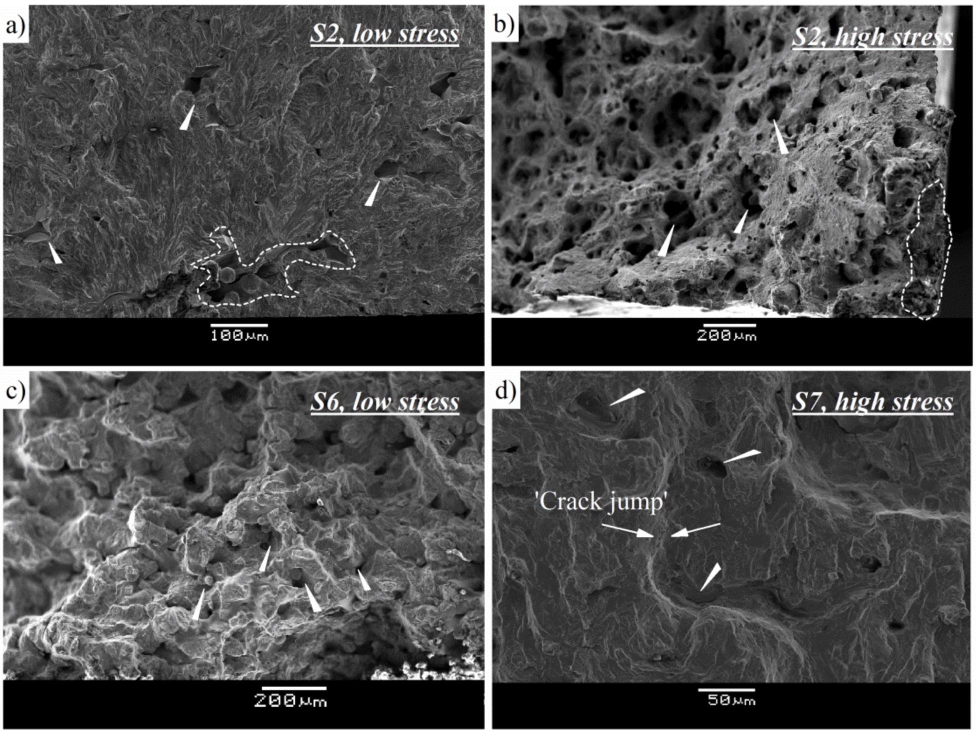

Figure 6 SEM fracture image of S2 (a) showing crack initiation from a subsurface lack of fusion pore (dash line) under the low applied stress; (b) it failed catastrophically under the high applied stress; (c) S6 failed via the brittle route even under the low applied stress; (d) secondary cracking occurred at lack of fusion pores in S7 under the high applied stress. Arrows indicate lack of fusion pores.

In addition, Figure 6d shows S7 under high stress, where crack fronts advanced individually from closely spaced lack of fusion defects and joined up with the main crack front to produce ‘crack jumps’.

Even though primary crack initiation in S7 is intergranular under both the high and low applied stress conditions, as discussed in Section 3.2.1, the lack of fusion defects were large enough to create sufficient local stress concentration such that secondary cracks were formed under the high applied stress. Pores in S3 were the second largest for specimens in the optimum processing region, at 14 μm; they could also have contributed to cracking in the bulk material. This explains the stronger effect of scan speed on high stress fatigue life: even though pores in S3 and S7 were benign under the low applied stress condition, they created sufficient stress concentration for cracking under the high applied stress and were responsible for the greater reduction in fatigue life. In fact, this explains the smaller amount of data scatter at high stress: crack initiation took place at uniformly distributed defects throughout the bulk material under high stress, whereas one or a few high stress concentrating defects are responsible for crack initiation under low stress. In the latter case, attributes of individual defects, such as orientation, size and location, as well as characteristics of neighbouring microstructure, are all relevant factors which could have resulted in the more probabilistic failure properties.

3.2.4 The true optimum processing condition

The correlation between fracture behaviour and cooling rate could explain the optimum processing condition being predicted at the lower left end of the process window: under low laser power, cooling rate increases, favouring intergranular crack initiation, which creates longer crack path and thereby longer fatigue life; further increase of the scan speed will trigger the transition to the under-melt region which is not favoured. However, consider the small processing region around S5. Since S5 does not contain critical crack initiating pores, the optimum region should occur slightly towards the higher scan speed end, where cooling rate could be further increased, rather than as that predicted by the regression model. Based on results from a prior work [37], for samples processed at condition marked by the unfilled dot in Figure 1, average values of $N_{\text{low stress}} = 5.9 \times 10^5$ cycles and $N_{\text{high stress}} = 4.3 \times 10^4$ cycles. Referring to the contour plots in Figure 3, the regression models correctly predict $N_{\text{high stress}}$, but underestimates $N_{\text{low stress}}$. This confirms the above prediction that cooling rate indeed relates directly with fatigue life under low cyclic stress. Under high cyclic stress, porosity contributed to cracking and the beneficial effect of high cooling rate diminished.

This result thus shows that the low stress fatigue life model does not predict the optimum processing condition accurately, mainly due to a lack of input data point in that region. Besides, the intricate relations between cooling rate and fracture behaviour could be responsible for the inadequacy of the second-order model for modelling low stress fatigue life, as indicated by the more significant lack-of-fit.

3.3 Processing-independent model

3.3.1 Model intuition

Considering the large number of L-PBF processing variables and the non-transferability of data across different systems, developing an effective data-driven processing model is challenging. A processing-independent fatigue stress-life prediction model is proposed in this section based on understanding of the fracture mechanisms, namely:

1) Mechanism 1: Fatigue crack initiation at microstructural heterogeneity in the absence of critical pores.
2) Mechanism 2: Fatigue crack initiation from lack of fusion pores, under the situations of
    a. Non-interacting pores

b. Interacting pores due to pore clustering

The Basquin equation was employed for representing the fatigue stress amplitude and cycles to failure relation:

$$\sigma_a = \sigma_f'(2N)^b \qquad (3)$$

where the fatigue strength coefficient σ_f’ and the fatigue strength exponent b are the intercept at $2N = 1$ and the slope of the logarithmic *S*-*N* plot respectively, and can be determined from zero mean stress tests ($R = -1$). For steel, σ_f’ is closely related to the monotonic tensile strength σ_b and is approximated by σ_f’ = σ_b [42, 43].

Figure 7a shows the tensile strength against the processing input energy density P/v of the samples. For the current process window and operating system, parts with tensile strength higher than 700 MPa could be produced under the optimum processing condition. Applying this strength criterion, the boundaries of the optimum region could be identified at S7 and S8, beyond which both under- and over-melting produced significantly deteriorated strength. Within the optimum region, tensile strength shows a steady reduction with input energy, as the slower cooling rate caused increased primary dendrite spacing in the solidified microstructure and lower strength [26]. For samples in the sub-optimum processing region, the reduced strength is due to either over-melting-induced material degradation (S4) or porosity (S2 and S6).

Figure 7b shows the relations between tensile strength and the *equivalent* fatigue strength parameters obtained at $R = 0.1$ in this work. (Note: The mean stress effect was not adjusted as *S*-*N* results could show significant variations depending on the adjustment method and data available [44]. Also, tests resulting in fatigue life < 10^3 cycles were not used for deriving σ_f’ and b.) It can be seen that σ_f’ indeed varies directly with σ_b. However, the resulting fatigue limit σ_e (fatigue strength at 10^6 cycles) shows different trend from σ_f’: despite the continuously increasing σ_f’ with σ_b, σ_e converges to a constant value with certain scattering for samples in the optimum processing region.

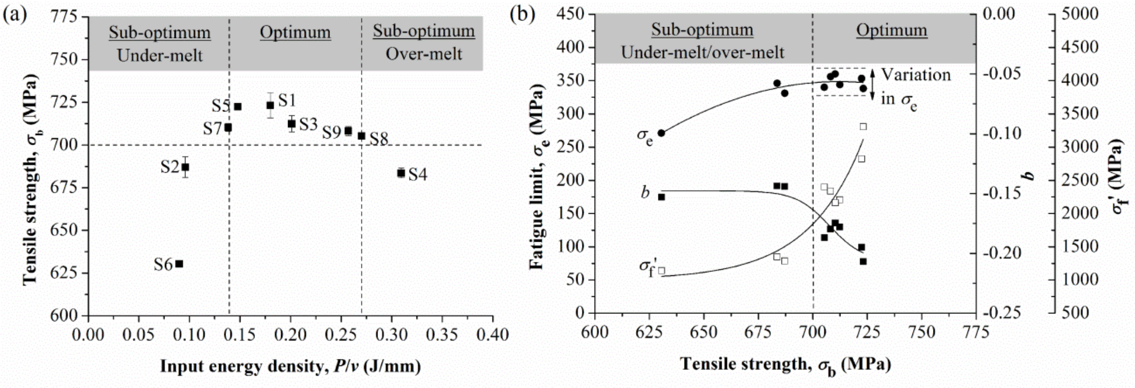

Figure 7 (a) Optimum and sub-optimum processing regions as identified by difference in tensile strength; (b) relations between tensile strength and the equivalent fatigue strength parameters and fatigue limits obtained at R = 0.1.

This is due to the opposing effect of b on fatigue resistance. As b is the slope of the *S*-*N* plot, it strongly affects long life performance: as b increases, the *S*-*N* slope becomes gentler and materials are more damage-tolerant. For the optimally processed samples where b decreases with increasing tensile strength, the *S*-*N* slopes are steeper, thereby retarding the increase in fatigue strength at long lives.

The opposing trend between b and σ_f' for ultrafine-grained alloys, as studied by Zhang et al., is related to grain size [45]. For the optimum samples, even though σ_f' increases due to grain refinement, b decreases as a result of the higher grain boundary density and microstructural instability. This explains the observed intergranular cracking, as described in Section 3.2.2, in a more simplistic manner without accounting for the intercellular particle effect and the transition to transgranular crack initiation. The scatter in fatigue limit values is therefore a reflection of the subtle changes in microstructure caused by variation in L-PBF processing conditions.

In real-life production, since this processing region produces high strength parts devoid of critical pores, any processing parameter combination in this region could be identified as the optimum condition. While the corresponding variations in microstructure and tensile strength are not easily detectable, the risk associated with finite life fatigue loading could be accounted for by applying an appropriate reduction factor on life or strength.

On the basis of the above relations between failure mechanism and fatigue strength parameters, the processing-independent fatigue prediction focuses on modelling of:

1) Mechanism 1 by deriving the reference *S-N* curve for representing the optimum behaviour of L-PBF stainless steel 316L. The scatter due to intrinsic microstructural changes is accounted for by the probability of failure parameter *Pr*.
2) Mechanism 2 by correlating porosity with the fatigue strength parameters to account for the effect of both interacting and non-interacting defects.

The effect of over-melting is not considered as the processing range tested in this work does not provide sufficient coverage of over-melting phenomena, e.g. over-melting pores and cracks, for modelling of fatigue failure in this processing region.

3.3.2 Modelling of mechanism 1

Figure 8a shows the *Pr-N* curves fitted to the experimental data, excluding S2, S4 and S6, for both the high and low stress conditions. The data for both stress conditions fit well to the lognormal distribution. The resulting *Pr-S-N* curves, corresponding to 5%, 50% and 95% probabilities of failure at 95% confidence level, are shown in Figure 8b. The mean-data curve can thus be modelled by the Basquin equation at 50% failure probability, with the equivalent values of σ_f' and b being 2560 MPa and -0.189 respectively. (Note: For purpose of comparison, based on the authors' unpublished work conducted at R = -1 for L-PBF stainless steel 316L, σ_f' and b equal to 1490 MPa and -0.123 respectively, whereas conventional stainless steel 316L adopts values of 660 MPa and -0.079 respectively [46].)

To cover for the 5% failure probability curve, a reduction factor of about 1.9 on life needs to be applied to the mean-data curve. Current ASME code fatigue design curves adopts a factor of 20 on life to estimate fatigue life for 95% of the population of austenitic stainless steel [47]. To account for the possible microstructural variations due to processing, an additional factor on the order of 1.9 is thus necessary for L-PBF-processed parts.

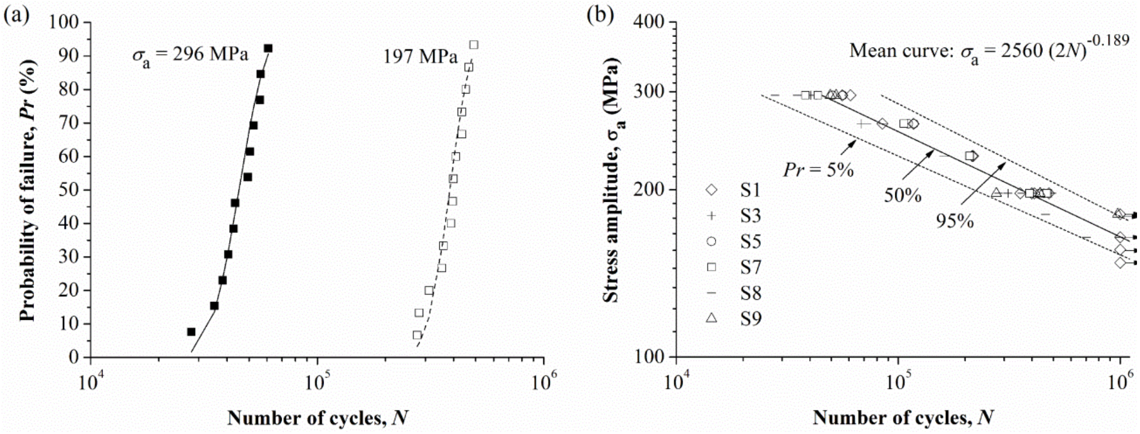

Figure 8 (a) Family of *Pr-N* curves plotted in terms of the lognormal distribution at applied stress amplitudes of 296 MPa and 197 MPa; (b) test data in the optimum processing region and reference *S-N* curves corresponding to 5%, 50% and 95% failure probabilities at 95% confidence level. The plots were obtained for *R* = 0.1.

3.3.3 Modelling of mechanism 2

Fatigue life is plotted against porosity fraction p and equivalent circular pore diameter $2a$ in Figure 9 for samples failed via mechanism 2. Porosity data for S7, denoted as S_{ref}, was used as a conservative estimate of the critical porosity condition for the transition between failure mechanisms 1 and 2, i.e. porosity fraction $p_{ref} = 0.05 \pm 0.03\%$ and equivalent circular pore diameter $2a_{ref} = 18.9 \pm 8.4$ μm. The fatigue life for S_{ref} was obtained from the reference *S-N* curve derived in Section 3.3.2. Comparing the relative effect of pore fraction and pore size, the latter corresponds to a more rapid reduction in fatigue life from S2 to S6. The same observation can be made for the high stress condition. To further analyse the *N-p* relations, the data points were approximated by power-law equations. As labelled in Figure 9, the exponent of the equation was estimated at -0.44 under the low stress condition, whereas under high stress, a smaller exponent of -1.39 was obtained.

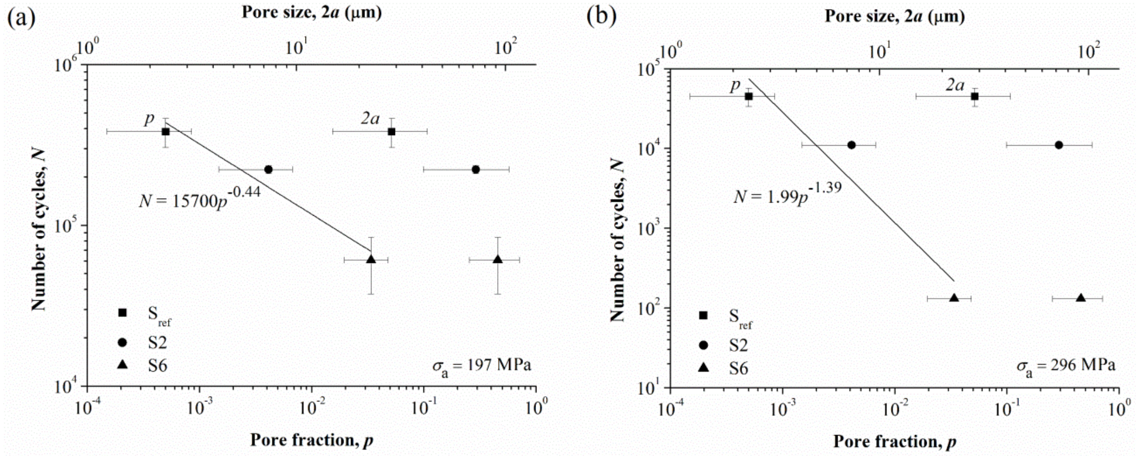

Figure 9 Fatigue life against porosity fraction and average extreme equivalent circular pore diameter for the (a) low stress and (b) high stress conditions.

To interpret this data, the nature of porosity in these samples needs to be evaluated. Due to the layer-layer process, defects generated within a single layer are replicated throughout the part as it is being built. With increasing under-melting, lack of fusion pores increase both in size and number. This lead to the aggregation effect [48], where not only the size of the defect, but also the quantity, impacts fatigue resistance. Specifically, the uniformly distributed pores could be represented by unit cells [49] of length d and circular pore radius a, as illustrated in Figure 10a, where porosity fraction is related to pore size by the equation:

$$p = \frac{\pi a^2}{d^2} \tag{4}$$

The interpore spacing λ is related to p and a as:

$$\lambda = d - 2a = \left(\sqrt{\frac{\pi}{p}} - 2\right) a \approx \sqrt{\frac{\pi}{p}}\, a \tag{5}$$

In a study by Holmes et al. [50], λ/a was referred to as the damage ratio, as it represents the space where stress can accumulate relative to the size of the stress concentrator. Thus, porosity fraction does not only account for the damaging effect of an isolated pore, but also its interaction with neighbouring pores. According to the BS 7910 for assessing the acceptability of flaws, when $\lambda \leq 2a$, adjacent flaws could be considered as interacting with an effective dimension equal to the summation of the individual flaw sizes and the interpore spacing. Optical micrographs in Figure 10b-d show typical pores (black regions) in S7, S2 and S6 respectively. It can be seen that while the maximum pores in both S2 and S6 could be comparable in size, pores in S6 are clearly interacting.

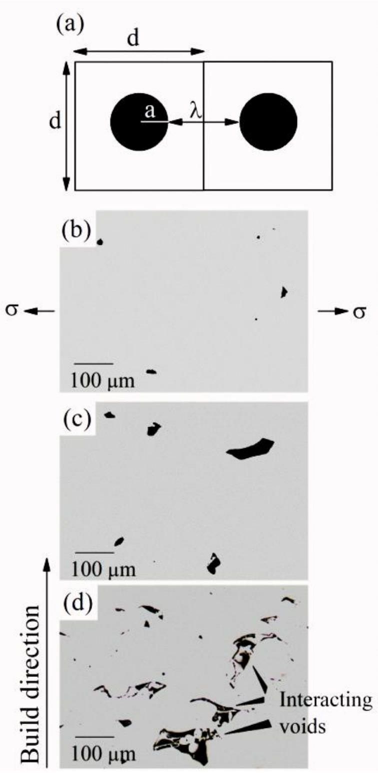

Figure 10 (a) Illustration of unit cells containing spherical voids. (b)-(d) Representative optical micrographs showing pores in S7, S2 and S6 respectively.

Consequently, for non-interacting pores in S2, the stress concentration effect of porosity is contingent on the characteristics of the initiating pores, whereas for S6, pore size determined from optical micrograph is smaller than the effective dimension of the interacting pores. This explains the more rapid reduction in fatigue life with pore size for S6.

For the high stress condition, the fatigue life of S6 decreases more rapidly as compared to the low stress condition, because the material was significantly overloaded such that catastrophic failure occurred after a small number of cycles.

The near inverse-square-root relation with porosity fraction, as indicated by the fitted lines in Figure 9a, is noteworthy. Replacing the p term by λ/a in the power-law equation according to Equation (5), it can be seen that fatigue life is in fact linearly related to the damage ratio λ/a. This provides a physical explanation to the observed power-law relation. However, as the relation estimates relatively high fatigue life as p approaches the fully porous condition (i.e. $p \rightarrow 1$), it is expected that such relation is only valid within a certain range of porosity fraction p_c. Beyond this, fatigue life will drop sharply due to significant reduction in load-bearing area and stronger interacting effect among the pores.

Based on this, for $p_{ref} < p < p_c$, the relation between porosity and high cycle fatigue life can be approximated by a power-law equation:

$$2N = mp^n \tag{6}$$

where m and n are stress-dependent; under low stress and high cycle fatigue, $n \approx -0.5$. Considering parts with porosity fractions p_1 and p_2, at the applied stress amplitude σ_a, Equation (3) leads to:

$$\sigma_a = \sigma'_{f1}(2N_1)^{b1} = \sigma'_{f2}(2N_2)^{b2} \tag{7}$$

As shown in Figure 7b, b increases sharply from the optimum to the sub-optimum processing region and remains nearly constant (approx. -0.144 to -0.153) with further reduction in strength. Thus, b can be assumed to adopt a constant value for failure via mechanism 2. Here, an equivalent value of -0.15 was assigned.

Combining Equations (6)-(7), the fatigue strength coefficient can be expressed as a function of the porosity fraction:

$$\sigma'_{f2} = (\frac{p_1}{p_2})^{nb}\sigma'_{f1} \approx (\frac{p_1}{p_2})^{0.075}\sigma'_{f1} \tag{8}$$

This expression predicts that for a part with increased porosity fraction, there will be a parallel downward shift of the *S-N* curve that is proportional to the log of the ratio between the porosity fractions. However, as the exponent 0.075 was calculated for the low stress case (n = -0.5), Equation (8) is expected to be more suited to low stress, long life fatigue prediction. In addition, it is to be emphasised that the power-law relation was approximated from a limited number of empirical results (Figure 9a). The applicability of this statistical relation for fatigue prediction is examined in the next section.

3.3.4 Model validation

The model was validated against test data listed in Table 3. Results from a prior work [51], labelled as T1-T3, were included to provide additional data for comparison. As they were fabricated by varying a different set of processing parameter, namely the layer thickness, they act to verify the processing-independency of the model.

For T1, $p = 0.04 \pm 0.05\%$ and $2a = 9.6 \pm 5.5$ μm. Both porosity parameters are less critical than that of S_{ref}, thus the sample is expected to fail via mechanism 1. Indeed, fractography analysis revealed intergranular crack initiation [51, 52]. The reference *Pr-S-N* curve was used to predict its fatigue properties. Referring to Figure 11a, the *S-N* data points of T1 are well covered by the 5% failure probability line. Applying the 1.9 reduction factor on life is thus conservative.

Table 3 Pore fraction, extreme equivalent circular pore size, crack initiation mechanism and the actual and predicted equivalent σ_f' values of the test samples.

Test samples	Pore fraction, p ($\times 10^{-2}$)	Pore size, $2a$ (μm)	Nature of crack initiation	Equivalent σ_f' at $R = 0.1$		
				Actual	Predicted	% error
S2	0.41 ± 0.26	42.1 ± 16.7	Mechanism 2	1286	1293	0.54
S6	3.38 ± 1.42	47.3 ± 12.4	Mechanism 2	1210	1104	-8.76
T1	0.04 ± 0.05	9.6 ± 5.5	Mechanism 1	1822	-	-
T2	0.70 ± 0.81	61.4 ± 39.4	Mechanism 2	1323	1243	-6.05
T3	10.85 ± 4.23	370.88 ± 178.04	Mechanism 2	897	1011	12.71

The rest of the samples contained critical pores and failed via mechanism 2. The equivalent fatigue strength coefficients were predicted from Equation (8). As listed in Table 3, the predicted values are in good agreement with the actual values, with less than 10% error, except for T3, where the model overestimated σ_f' by 13%. Figure 11b compares the predicted fatigue life with the experimental data obtained at different applied cyclic loading. It can be seen that except for T3, the predicted fatigue lives are generally within a factor of two of the experimental results (dash lines). Considering the inherent data scatter, Equation (8), despite being derived for the low stress condition, provides reasonable prediction for higher applied stresses, e.g. data points with life lower than 10^5 cycles. For T3, the model overestimates the fatigue life by a factor of about 10. This indicates that the porosity fraction of T3 is larger than p_c such that the inverse-square-root relation is not valid.

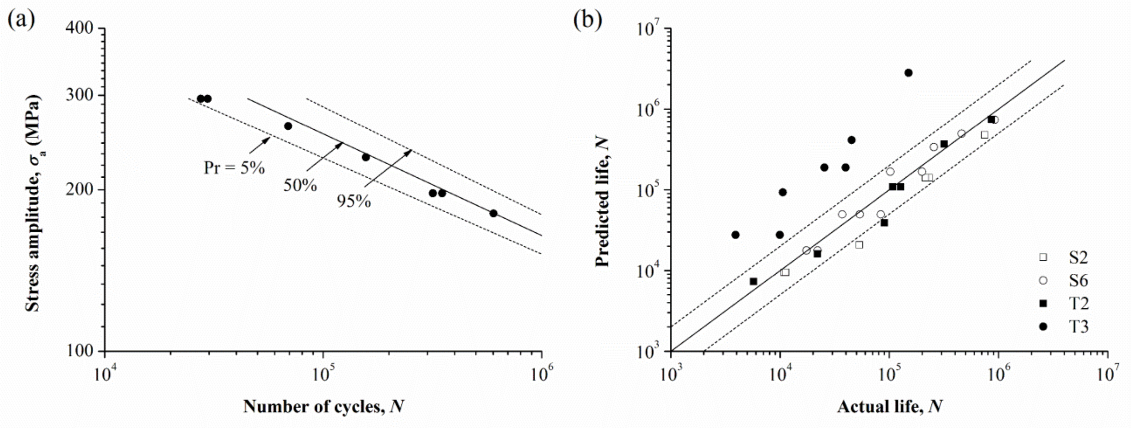

Figure 11 (a) *S-N* data of T1 are within the 5% failure probability band for failure by mechanism 1; (b) predicted versus test measured fatigue life data of S2, S6, T2 and T3 which failed by mechanism 2.

The results are satisfactory, especially considering that it predicted well for the data set of T2, which was not used in the model derivation. However, the validity and uncertainty associated with the power-law relation between fatigue life and porosity fraction remains to be further investigated and supported by experimental results. Also, it is to be noted that since fatigue strength is related to tensile strength, the fatigue strength parameters obtained in this work applies to parts with comparable tensile strength, as that shown in Figure 7. For parts belonging to different strength regimes, e.g. due to processing at higher layer thickness where grain coarsening could cause a general reduction of material strength [53], adjustment factors may need to be applied.

3.4 Generalisation capability of the models – Validation with literature

As both the processing-dependent and processing-independent models were developed based on the authors' own experimental data, their predictive capabilities are further demonstrated in this section using data from literature. The relevant input data are listed in Table 4. Several assumptions and adjustments were made to the test data to account for the different sample preparation and testing conditions, and they are described in the following paragraphs.

Table 4 Input information from literature for validating the processing-(in)dependent models.

Sources	Laser power, P (W)	Scan speed, v (mm/s)	Nature of crack initiation
Spierings et al. [54]	103	425	-
Shrestha et al. [12]	400	1000	Mechanism 2
Mower et al. [55]	195	750	Surface roughness

For the processing-dependent model, the regression equations do not account for variables other than laser power and scan speed. One of the key variables that was not kept constant across the studies is layer thickness: higher layer thicknesses, i.e. 30 μm [12, 54] and 40 μm [55], were used in the references, whereas samples in this work were prepared at 20 μm. Based on the authors' prior study [52], the P-v combination used for fabricating S1 could produce sufficient laser penetration such that critical pores were not generated at 40 μm layer thickness, and the fatigue properties of the samples built at 20 μm and 40 μm were similar. Based on this fact, some tolerance for variations in layer thickness setting could be allowed. For example, though the samples used by Mower et al. [55] were fabricated at 40 μm layer thickness, the P-v values are close to S1 (Figure 3c). Thereby, no significant shift in the processing region is expected. For the other two works, the deviation in layer thickness is even smaller and was assumed to produce negligible effect.

Quantitative information of porosity fraction was not provided in the references for direct application of the processing-independent approach. By examining the fractographs, fatigue failure occurred via mechanism 2 for the samples tested by Shrestha et al. [12], with major cracks originating from lack of fusion defects on the order of 200 μm. For the work by Mower et al., samples were tested in the as-built condition without machining, and failure were triggered by fabrication defects on the surface. Based on the fractographs provided, the surface defects are smaller but more closely spaced than the lack of fusion defects (measured average surface roughness of 5-6 μm). For the work by Spierings et al. [54], information on the failure mechanism was not available. Nonetheless, as similar *S*-*N* curves were obtained for samples with different surface finishes (as-machined versus machined and polished samples), it was speculated by the authors that factors such as internal pores could be driving the fatigue failure.

For comparing the fatigue test data, the Goodman equation was applied to the test data by Mower et al. as they were obtained at $R = -1$. Also, a modifying factor of 0.85 on fatigue strength was applied to adjust for the bending load [56]. Fatigue test results from Shrestha et al. were only used for qualitative analysis and not quantitatively as the tests were done in strain-controlled mode. In addition, vertically-built samples were tested by Spierings et al., whereas data for horizontal samples were adapted from the other studies. Nonetheless, based on the results of Shrestha et al. [12] and the authors' unpublished works, build orientation is not a significant factor on the high cycle fatigue properties of L-PBF stainless steel 316L.

Results for comparing the processing-dependent models are shown in Figure 12a. The predicted fatigue life exceeded the test results of Spierings et al. by more than an order of magnitude. As discussed in Section 3.2.4, the over-estimated fatigue life at low laser power and scan speed is because of the lack of sufficient data points tested in the region. Also, as the parameter settings used in this work are significantly beyond the presently tested processing window, the poor correlation indicates that the regression equations are only valid within the experimentally tested working range. For the processing parameters used by Shrestha et al., negative fatigue lives were predicted under both the low and high stress conditions. It is interesting that while the process map in Figure 3c predicts over-melting, lack of fusion defects were reported by Shrestha et al. The inability to predict the processing region correctly is evident of the non-transferability of processing information across L-PBF machines, which could be due to different gas flow designs and laser units.

Machines from the same manufacturer and similar processing parameters were used by Mower et al. and this work. As shown in Figure 12a, the regression model provides reasonable estimates of the S-N relation, except for the two data points with the shortest fatigue lives. According to the process map in Figure 3c, the processing condition should produce optimum samples. As the surface roughness-induced defects are smaller than the lack of fusion defects, they could be less damaging and caused equivalent stress concentration effect as the microstructural defects. Consequently, the regression models could accurately predict the fatigue test results of Mower et al. even though the samples were not machined. The outliers at shorter fatigue life could be attributed to the use of fully reversed fatigue tests (R = -1) where the cyclic tension-compression action inflicted severer damage [57], especially at higher stress amplitudes, than the tension-tension tests (R = 0.1) performed by Spierings et al. and this work.

The effectiveness of the processing-independent model is demonstrated in Figure 12b. Lines of constant porosity fraction, obtained by applying Equation (8), were plotted on the fatigue stress-life axes. Agreeing with results from the regression model, test data by Mower et al. are comparable to those of the optimum samples in this work, i.e. most of the data points are close to and above the $p = p_{\text{ref}} = 0.05\%$ line. For the results by Spierings et al., most of the data points are covered by the $p = 0.1\%$ and $p = 1\%$ lines. This indicates that crack initiation could have occurred via mechanism 2, thereby testifying to the speculation of the authors that internal pores could be responsible for the similar fatigue properties between the samples with different surface finishes. The large amount of scatter in the test data could indicate inconsistency of the build process, which had led to nonhomogeneous porosity distribution of the samples.

In summary, the processing-dependent regression models provide good prediction for parts made by the same L-PBF machine as this work. Its applicability is also confined to the presently tested processing window. The processing-independent approach is not affected by such restrictions; it provides effective predictions of the fatigue fracture mechanism regardless of the processing condition.

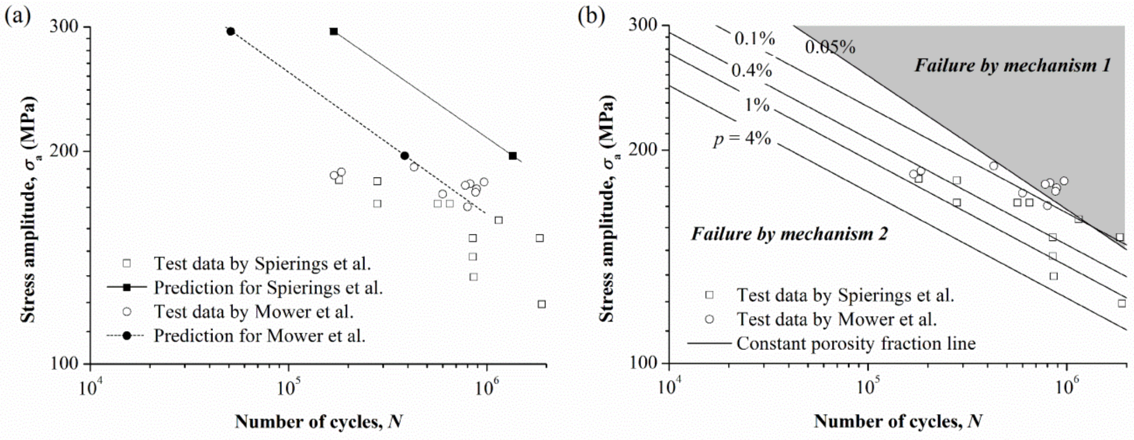

Figure 12 Comparing fatigue test data from literature with predicted results obtained from (a) processing-dependent regression model and (b) processing-independent model. The plots were obtained for *R* = 0.1.

4. Conclusions

Fatigue properties of stainless steel 316L made by the laser powder bed fusion process under controlled changes in laser power and scan speed were studied by employing the statistical response surface method. Results from this work show that a complex relationship exists between processing, loading condition and fatigue failure. In developing predictive models for the fatigue stress-life relations, the following conclusions could be made:

1) The second-order polynomial equation predicts well the influence of laser power and scan speed on high stress fatigue life. For low stress, high cycle fatigue, the model produces poorer performance and a higher-order model could be desirable.

2) The fatigue fracture mechanisms responsible for the observed behaviours were evaluated. Under low stress, damage builds up gradually over a large number of cycles. In the absence of critical pores, microstructure defects are the weakest links and cause crack initiation. As the microstructure-driven fatigue failure is sensitive to changes in cooling rate and the competing effect of porosity, higher-order equations are necessary for modelling the processing-dependent fatigue properties. As the cyclic stress increases, processing-induced defects, either porosity or material degradation, affect fatigue properties more strongly, such that a more distinct relationship exists between processing and fatigue life, which could be effectively modelled by the second-order equation.

3) From an engineering standpoint, the fatigue failure behaviour indicates that: a) with optimum processing and low loading stress, microstructure-driven failure promotes enhanced tolerance for porosity such that gas pores, even small lack of fusion defects, do not need to be controlled as they are not detrimental to crack initiation; b) for finite life, especially high stress applications, processing needs to be closely monitored to prevent porosity and strength degradation, which strongly affects short life fatigue resistance.

4) A processing-independent model was proposed for predicting the stress-life relations of both the microstructure-driven and porosity-driven fatigue failure modes. For the microstructure-driven failure, the optimum fatigue properties were modelled by a reference *S*-*N* curve, where the effect

of subtle variations in microstructure was accounted for by applying a reduction factor of 1.9 on life. For the porosity-driven failure, the available test data led to the assumption of an inverse-square-root relation between fatigue life and porosity fraction, which was incorporated into the Basquin equation for predicting the fatigue strength coefficient. As this relation was obtained based on limited test data, its validity remains to be further investigated.

5) The models were cross-validated against data from literature to demonstrate the generalisation capability. The processing-dependent regression model produced reasonable results for samples that were made using similar machines and processing conditions as this work, indicating that its applicability is indeed machine- and processing region-dependent. The processing-independent model accurately predicted the fatigue fracture mechanisms, i.e. porosity- or microstructure-driven failure, regardless of the processing conditions. Quantitative confirmation of the porosity-fatigue properties relation was not possible due to a lack of porosity information of the test samples.

Acknowledgement

This work was supported by the Singapore Economic Development Board (EDB) Industrial Postgraduate Programme (IPP).

References

[1] J. Cherry, H. Davies, S. Mehmood, N. Lavery, S. Brown, J. Sienz, Investigation into the effect of process parameters on microstructural and physical properties of 316L stainless steel parts by selective laser melting, Int. J. Adv. Manuf. Technol. 76(5-8) (2015) 869-879.
[2] J. Sun, Y. Yang, D. Wang, Parametric optimization of selective laser melting for forming Ti6Al4V samples by Taguchi method, Opt. Laser Technol. 49 (2013) 118-124.
[3] H.-T. Liao, J.-R. Shie, Optimization on selective laser sintering of metallic powder via design of experiments method, Rapid Prototyping Journal 13(3) (2007) 156-162.
[4] N. Read, W. Wang, K. Essa, M.M. Attallah, Selective laser melting of AlSi10Mg alloy: Process optimisation and mechanical properties development, Materials & Design (1980-2015) 65 (2015) 417-424.
[5] P. Bacchewar, S. Singhal, P. Pandey, Statistical modelling and optimization of surface roughness in the selective laser sintering process, Proceedings of the Institution of Mechanical Engineers, Part B: Journal of Engineering Manufacture 221(1) (2007) 35-52.
[6] C. Kamath, Data mining and statistical inference in selective laser melting, Int. J. Adv. Manuf. Technol. 86(5-8) (2016) 1659-1677.
[7] G. Tapia, S. Khairallah, M. Matthews, W.E. King, A. Elwany, Gaussian process-based surrogate modeling framework for process planning in laser powder-bed fusion additive manufacturing of 316L stainless steel, Int. J. Adv. Manuf. Technol. (2017) 1-13.
[8] A.M. Aboutaleb, L. Bian, A. Elwany, N. Shamsaei, S.M. Thompson, G. Tapia, Accelerated process optimization for laser-based additive manufacturing by leveraging similar prior studies, IISE Transactions 49(1) (2017) 31-44.
[9] K.F. Walker, Q. Liu, M. Brandt, Evaluation of fatigue crack propagation behaviour in Ti-6Al-4V manufactured by selective laser melting, Int. J. Fatigue 104(Supplement C) (2017) 302-308.
[10] P. Edwards, M. Ramulu, Effect of build direction on the fracture toughness and fatigue crack growth in selective laser melted Ti‐6Al‐4 V, Fatigue Fract. Eng. Mater. Struct. 38(10) (2015) 1228-1236.
[11] M. Tang, P.C. Pistorius, Oxides, porosity and fatigue performance of AlSi10Mg parts produced by selective laser melting, Int. J. Fatigue 94 (2017) 192-201.
[12] R. Shrestha, J. Simsiriwong, N. Shamsaei, S.M. Thompson, L. Bian, Effect of build orientation on the fatigue behavior of stainless steel 316l manufactured via a laser-powder bed fusion process.

[13] A. Yadollahi, N. Shamsaei, S.M. Thompson, A. Elwany, L. Bian, Effects of building orientation and heat treatment on fatigue behavior of selective laser melted 17-4 PH stainless steel, Int. J. Fatigue 94 (2017) 218-235.
[14] M. Akita, Y. Uematsu, T. Kakiuchi, M. Nakajima, R. Kawaguchi, Defect-dominated fatigue behavior in type 630 stainless steel fabricated by selective laser melting, Mater. Sci. Eng., A 666 (2016) 19-26.
[15] E. Brandl, U. Heckenberger, V. Holzinger, D. Buchbinder, Additive manufactured AlSi10Mg samples using Selective Laser Melting (SLM): Microstructure, high cycle fatigue, and fracture behavior, Mater. Des. 34 (2012) 159-169.
[16] E. Wycisk, A. Solbach, S. Siddique, D. Herzog, F. Walther, C. Emmelmann, Effects of defects in laser additive manufactured Ti-6Al-4V on fatigue properties, Physics Procedia 56 (2014) 371-378.
[17] K. Darvish, Z.W. Chen, T. Pasang, Reducing lack of fusion during selective laser melting of CoCrMo alloy: Effect of laser power on geometrical features of tracks, Mater. Des. 112 (2016) 357-366.
[18] R.H. Myers, D.C. Montgomery, C.M. Anderson-Cook, Response surface methodology: process and product optimization using designed experiments, John Wiley & Sons2016.
[19] G. Miranda, S. Faria, F. Bartolomeu, E. Pinto, S. Madeira, A. Mateus, P. Carreira, N. Alves, F.S. Silva, O. Carvalho, Predictive models for physical and mechanical properties of 316L stainless steel produced by selective laser melting, Mater. Sci. Eng., A 657 (2016) 43-56.
[20] Y. Murakami, Effects of small defects and nonmetallic inclusions on the fatigue strength of metals, JSME international journal. Ser. 1, Solid mechanics, strength of materials 32(2) (1989) 167-180.
[21] X. Zhu, J. Yi, J. Jones, J. Allison, A probabilistic model of fatigue strength controlled by porosity population in a 319-type cast aluminum alloy: Part I. Model Development, Metall. Mater. Trans. A 38(5) (2007) 1111-1122.
[22] S. Tammas-Williams, P. Withers, I. Todd, P. Prangnell, The Influence of Porosity on Fatigue Crack Initiation in Additively Manufactured Titanium Components, Scientific Reports 7 (2017).
[23] P. Portella, K.-T. Rie, Low cycle fatigue and elasto-plastic behaviour of materials, Elsevier1998.
[24] L. Pook, Why Metal Fatigue Matters, Springer2007.
[25] W. Shifeng, L. Shuai, W. Qingsong, C. Yan, Z. Sheng, S. Yusheng, Effect of molten pool boundaries on the mechanical properties of selective laser melting parts, J. Mater. Process. Technol. 214(11) (2014) 2660-2667.
[26] D. Wang, C. Song, Y. Yang, Y. Bai, Investigation of crystal growth mechanism during selective laser melting and mechanical property characterization of 316L stainless steel parts, Mater. Des. 100 (2016) 291-299.
[27] M.H. Yoo, A.H. King, Intergranular fracture by slip/grain boundary interaction, Metall. Trans. A 21(9) (1990) 2431-2436.
[28] Z. Zhang, Z. Wang, Dependence of intergranular fatigue cracking on the interactions of persistent slip bands with grain boundaries, Acta Mater. 51(2) (2003) 347-364.
[29] Y. Zhong, L. Liu, S. Wikman, D. Cui, Z. Shen, Intragranular cellular segregation network structure strengthening 316L stainless steel prepared by selective laser melting, J. Nucl. Mater. 470 (2016) 170-178.
[30] J.-P. Kruth, G. Levy, F. Klocke, T. Childs, Consolidation phenomena in laser and powder-bed based layered manufacturing, CIRP Annals-Manufacturing Technology 56(2) (2007) 730-759.
[31] M. Pridantsev, F. Levin, Effect of manganese on the structure and properties of nonmagnetic stainless steels, Metal Science and Heat Treatment 7(12) (1966) 786-789.
[32] A.I.Z. Farahat, O. Hamed, A. El-Sisi, M. Hawash, Effect of hot forging and Mn content on austenitic stainless steel containing high carbon, Mater. Sci. Eng., A 530(Supplement C) (2011) 98-106.
[33] T. Mukherjee, J. Zuback, A. De, T. DebRoy, Printability of alloys for additive manufacturing, Scientific reports 6 (2016).
[34] W.E. King, H.D. Barth, V.M. Castillo, G.F. Gallegos, J.W. Gibbs, D.E. Hahn, C. Kamath, A.M. Rubenchik, Observation of keyhole-mode laser melting in laser powder-bed fusion additive manufacturing, J. Mater. Process. Technol. 214(12) (2014) 2915-2925.
[35] Y. Liu, Y. Yang, S. Mai, D. Wang, C. Song, Investigation into spatter behavior during selective laser melting of AISI 316L stainless steel powder, Mater. Des. 87 (2015) 797-806.

[36] Y. Liu, Y. Yang, D. Wang, A study on the residual stress during selective laser melting (SLM) of metallic powder, Int. J. Adv. Manuf. Technol. 87(1-4) (2016) 647-656.
[37] M. Zhang, C.-N. Sun, X. Zhang, P.C. Goh, J. Wei, D. Hardacre, H. Li, Fatigue and fracture behaviour of laser powder bed fusion stainless steel 316L: Influence of processing parameters, Mater. Sci. Eng., A 703 (2017) 251-261.
[38] K.V. Yang, P. Rometsch, T. Jarvis, J. Rao, S. Cao, C. Davies, X. Wu, Porosity formation mechanisms and fatigue response in Al-Si-Mg alloys made by selective laser melting, Mater. Sci. Eng., A.
[39] T. Amine, J.W. Newkirk, F. Liou, An investigation of the effect of direct metal deposition parameters on the characteristics of the deposited layers, Case Studies in Thermal Engineering 3 (2014) 21-34.
[40] M.H. Farshidianfar, A. Khajepour, A.P. Gerlich, Effect of real-time cooling rate on microstructure in Laser Additive Manufacturing, J. Mater. Process. Technol. 231(Supplement C) (2016) 468-478.
[41] Q. Wang, Microstructural effects on the tensile and fracture behavior of aluminum casting alloys A356/357, Metall. Mater. Trans. A 34(12) (2003) 2887-2899.
[42] R.W. Landgraf, Cyclic deformation and fatigue behavior of hardened steels, Department of Theoretical and Applied Mechanics (UIUC), 1968.
[43] R. Landgraf, The resistance of metals to cyclic deformation, Achievement of High Fatigue Resistance in Metals and Alloys, ASTM International1970.
[44] N.E. Dowling, Mean stress effects in stress-life and strain-life fatigue, SAE Technical Paper, 2004.
[45] Z. Zhang, J. Pang, Z. Zhang, Optimizing the fatigue strength of ultrafine-grained Cu-Zn alloys, Mater. Sci. Eng., A 666 (2016) 305-313.
[46] B. Boardman, Fatigue Resistance of Steels, Properties and Selection: Irons, Steels, and High-Performance Alloys, ASM Handbook, ASM International1990, pp. 673–688.
[47] M. Dahlberg, D. Bremberg, Fatigue margins for austenitic stainless steels in ASME Boiler and pressure vessel code–a literature study, Stral Sakerhets Myndigheten Swedish Radiation Safety Authority (2012).
[48] H.R. Ammar, A.M. Samuel, F.H. Samuel, Effect of casting imperfections on the fatigue life of 319-F and A356-T6 Al–Si casting alloys, Mater. Sci. Eng., A 473(1) (2008) 65-75.
[49] Q. Zhang, Z. Zuo, J. Liu, Numerical analysis for the influence of casting micro porosity on fatigue life, Engineering Failure Analysis 48(Supplement C) (2015) 11-20.
[50] J. Holmes, R. Queeney, Fatigue crack initiation in a porous steel, Powder Metall. 28(4) (1985) 231-235.
[51] M. Zhang, C.-N. Sun, X. Zhang, P.C. Goh, J. Wei, H. Li, D. Hardacre, Elucidating the Relations Between Monotonic and Fatigue Properties of Laser Powder Bed Fusion Stainless Steel 316L, JOM 1-6.
[52] M. Zhang, C.-N. Sun, X. Zhang, P.C. Goh, J. Wei, H. Li, D. Hardacre, Competing influence of porosity and microstructure on the fatigue property of laser powder bed fusion stainless steel 316l, Solid Freeform Fabrication Symposium, University of Texas Austin, USA, 2017.
[53] M. Ma, Z. Wang, M. Gao, X. Zeng, Layer thickness dependence of performance in high-power selective laser melting of 1Cr18Ni9Ti stainless steel, J. Mater. Process. Technol. 215 (2015) 142-150.
[54] A. Spierings, T. Starr, K. Wegener, Fatigue performance of additive manufactured metallic parts, Rapid Prototyping Journal 19(2) (2013) 88-94.
[55] T.M. Mower, M.J. Long, Mechanical behavior of additive manufactured, powder-bed laser-fused materials, Mater. Sci. Eng., A 651 (2016) 198-213.
[56] L. Prasad, Handbook of mechanical design, Tata McGraw-Hill Education1995.
[57] J.-Y. Huang, J.-J. Yeh, S.-L. Jeng, C.-Y. Chen, R.-C. Kuo, High-cycle fatigue behavior of type 316L stainless steel, Materials transactions 47(2) (2006) 409-417.